GPS Solutions (2023) 27:102
https://doi.org/10.1007/s10291-023-01445-1

RESEARCH

Effect of GNSS radio occultation observations on the prediction of the 2021 Henan rainstorm

Yu Wang[1,2] · **Shuanggen Jin**[1,3]

Received: 1 December 2022 / Accepted: 23 March 2023

Abstract
Accurately predicting heavy rainstorms remains challenging due to limited spatial and temporal measurements. Nowadays, space-borne Global Navigation Satellite System (GNSS) radio occultation (RO) data provides high spatial-resolution atmospheric parameters, which can improve the precision of heavy rainfall prediction. This study investigates the impact of GNSS radio occultation observations on forecasting the extremely heavy rainfall that occurred in Henan, China, on July 20, 2021. We assimilate GNSS radio occultation data from Constellation Observing System for Meteorology, Ionosphere, and Climate-2 (COSMIC-2), MetOp-A/B/C, and Fengyun (FY)-3C GNOS in Weather Research and Forecasting Model Data Assimilation (WRFDA) three-dimensional framework (3DVAR) system, using the local refractivity operator. Control experiment (CNTL) and RO are designed to assess the impact of GNSS radio occultation on this extreme rainfall prediction, and RO + GNOS is conducted to further evaluate the influence of GNSS RO data onboard FY-3C. The fractions skill score (FSS) is used to quantify the accuracy of predicted precipitation at given thresholds. The results demonstrate that assimilating GNSS radio occultation data improves precipitation forecasts in terms of the distribution and quantity, due to more precise initial conditions for the moisture field. The study also finds that RO and RO + GNOS produce similar increments and outperform the CNTL, indicating a more accurate humidity field near Henan and more explicit water vapor channels. Moreover, the study reveals that assimilating additional data from GNOS onboard FY-3C significantly enhances the prediction of this record-breaking rainfall.

Keywords GNSS · Radio occultation · GNOS · Weather forecast · Extreme rainfall

Introduction

Extreme precipitation events often significantly damage society, including casualties and property losses, surpassing the impact of most other meteorological events (Wang et al. 2021; Zhang and Zhou 2020). According to the Clausius–Clapeyron equation, the atmospheric saturation vapor pressure will increase by 7% for every degree rise in temperature (Rhys et al. 2010; Trenberth et al. 2003). Hence, the intensity and frequency of extreme precipitation have significantly increased due to global warming (Berg et al. 2013; Lenderink and van Meijgaard 2008; Westra et al. 2013). Moreover, climate projections suggest that these extreme precipitation events are likely to increase further in the future due to additional warming (Chen et al. 2012; Prein et al. 2016). Thus, it is critical to improving the forecast skill for extreme precipitation to mitigate the associated societal and environmental impacts.

The quality of initial conditions is a fundamental factor affecting the accuracy of weather forecasts (Kimura 2002; Leith 1978; Privé and Errico 2013). Among the variables that comprise initial conditions, the moisture field is especially critical for accurate precipitation forecasts. Unfortunately, conventional observational techniques for vertical profiles, which rely primarily on radiosondes, suffer from low temporal resolution and uneven spatial distribution worldwide. (Anisetty et al. 2013). As a result, initial conditions often inadequately capture the true state of the atmosphere, leading to significant errors in precipitation

✉ Shuanggen Jin
sgjin@shao.ac.cn

[1] Shanghai Astronomical Observatory, Chinese Academy of Sciences, Shanghai 200030, China

[2] School of Astronomy and Space Science, University of Chinese Academy of Sciences, Beijing 100049, China

[3] School of Surveying and Land Information Engineering, Henan Polytechnic University, Jiaozuo 454000, China

Published online: 11 April 2023

forecasting. However, the rapid development of the Global Navigation Satellite System (GNSS) has yielded promising advances in meteorological monitoring and forecasting (Dong and Jin 2018; Jin et al. 2022; Jin and Su 2020; Jin and Zhang 2016). In particular, GNSS radio occultation measurements offer several advantages, including exceptional accuracy, high vertical resolution, absence of instrument drifting, and all-weather sounding capability, as well as global coverage (Anthes 2011; Kursinski et al. 2000). One noteworthy example of this technology is the Constellation Observing Systems for Meteorology, Ionosphere and Climate (COSMIC), an important international satellite project that provides high-quality radio occultation profiles globally (Ho et al. 2020). These profiles have been widely used in operational weather prediction, climate analysis, and space weather forecasting. Consequently, a follow-on operational mission called COSMIC-2 was launched in 2019 to continue the success of the project (Anthes and Schreiner 2019). In addition to COSMIC-2, other operational meteorological satellites, such as MetOp-A/B/C from the European Space Agency (ESA) and Fengyun (FY)-3C from China, are equipped with radio occultation instruments, which serve to expand the use of this promising technology.

Several experiments have confirmed the substantial enhancement in weather forecast accuracy for temperature (Healy 2008), frontal precipitation (Chien and Kuo 2009), and cyclones (Anisetty et al. 2013; Chen et al. 2009; Huang et al. 2005) when using GNSS radio occultation data. However, few studies have explored the impact of GNSS radio occultation data on predicting extreme rainfall events. Furthermore, previous studies primarily relied on data from COSMIC and MetOp satellites, with limited utilization of GNSS radio occultation data from China's FY-3C. The benefit of assimilating this data into numerical weather prediction has not been comprehensively demonstrated and needs further investigation. This study aims to investigate the effect of GNSS radio occultation refractivity on simulations of an extreme rainfall event that occurred in Henan, China, in July 2021. The GNSS radio occultation data utilized in this study consist of refractivity from COSMIC2, MetOp-A/B/C, and FY-3C satellites.

Data and methods

This section gives an overview of the Henan extreme rainstorm case and presents the datasets and methods employed in this study. The datasets used, including observations, model products, and GNSS radio occultation data, will be presented in full detail. The assimilation, forecast, and evaluation processes will be thoroughly described.

July 2021 Henan extreme heavy rainstorm

In July 2021, central China's Henan Province experienced a devastating rainstorm resulting in significant economic losses and a high number of casualties. According to the China Meteorological Administration, more than 100 mm of precipitation was recorded at 794 meteorological stations in Henan on July 19, with 32.5% of the area of the province receiving more than 250 mm of accumulated rainfall. (Cheng et al. 2022; Yin et al. 2022). Zhengzhou, the capital city of Henan, was hit particularly hard, receiving an unprecedented 552.5 mm of rainfall within 24 h. The heavy rains caused severe waterlogging, traffic disruptions, and power outages. The most intense rainfall occurred from 0600 to 1000 UTC on July 20, with a record-breaking hourly precipitation of 201.9 mm recorded at Zhengzhou station during 0800–0900 UTC on that day.

Precipitation products and reanalysis data

The calibrated satellite-based precipitation data provided by the Integrated Multi-satellite Retrievals for Global Precipitation Measurement Mission (IMERG) is applied as observation for this study (Huffman et al. 2019). The IMERG products are obtained from a constellation of satellites by using a sustainable multi-satellite algorithm that amalgamates the strengths of prior algorithms (Wolff et al. 2007). IMERG provides high-precision products with a spatial resolution of $0.1°\times 0.1°$ at half-hour intervals. IMERG products are available in three types: early run, late run, and final run products. The early, late, and final run offer multi-satellite precipitation estimates with latencies of 4 h, 12–24 h, and 3.5 months, respectively. The key difference between these products lies in their propagation methods, with the early run featuring forward propagation only, while the late run includes both forward and backward propagation for interpolation. The final run product incorporates monthly gauge data for higher-quality results and is particularly suitable for research purposes.

ERA5 reanalysis data (Hersbach et al. 2018) at a horizontal resolution of $0.1°\times 0.1°$ and 37 vertical layers during July 19–20, 2021 are used to identify synoptic patterns and verify the impact of GNSS radio occultation on assimilations. The European Centre provides the dataset for Medium-Range Weather Forecast (ECMWF).

The Global Forecast System (GFS) is a National Centers for Environmental Prediction (NCEP) weather forecast model that generates data for dozens of atmospheric variables at a resolution of $0.25°\times 0.25°$. Conventional data used in this study are from the Global Telecommunications System (GTS).

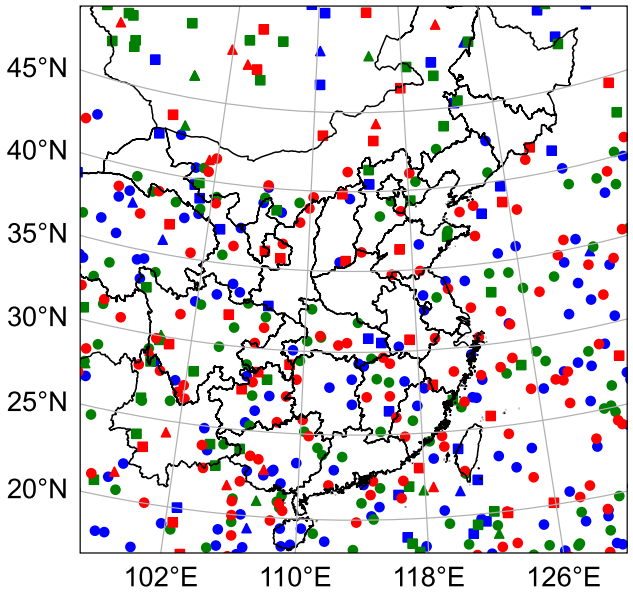

Fig. 1 Map of GNSS radio occultation soundings from COSMIC2 (circles), MetOp (squares), and FY-3C (triangles) on July 17 (blue), 18 (green), and 19 (red)

GNSS radio occultation refractivity data

The GNSS radio occultation soundings used in this study are mainly obtained from the Constellation Observing System for Meteorology, Ionosphere, and Climate-2 (COSMIC-2). COSMIC-2 is a joint mission between Taiwan and the United States aimed at demonstrating the value of GNSS radio occultation data in operational weather prediction, climate analysis, and space weather forecasts. The mission has launched six satellites with next-generation GNSS radio occultation payloads into low earth orbit, generating up to 5000 soundings per day (Schreiner et al. 2020). In addition to COSMIC-2, radio occultation soundings from the MetOp-A/B/C and FY-3C satellites are also employed in this study. MetOp satellites equipped with GNSS receivers called GRAS have been launched since 2006 and can collect approximately 650 soundings per day (von Engeln et al. 2011). The FY-3C is the first Chinese satellite capable of using the radio occultation technique to obtain atmospheric profiles. Its GNSS receiver onboard, called the GNSS Occultation Sounder (GNOS), can receive signals from both GPS and BeiDou navigation satellite System (BDS) constellations, providing around 500 soundings per day (Bai et al. 2014; Bi et al. 2012; Jin et al. 2019). As depicted in Fig. 1, the distribution of soundings used in this study is widespread, including 322 soundings from COSMIC-2, 98 from MetOp, and 27 from FY-3C, and are randomly scattered throughout the simulation domain. On average, there are approximately 149 GNSS-RO soundings per day.

There are several assimilable products of GNSS radio occultation, including bending angle, refractivity, and meteorological variables derived therefrom, such as pressure, temperature, and water vapor mixing ratio. Previous studies suggested using a local refractivity operator for assimilation after prudently balancing computational cost and horizontal errors (Ha et al. 2014). Therefore, we employ the local refractivity operator in this study. The neutral atmospheric refractivity is described by Smith and Weintraub (1953) and is used to calculate the innovation:

$$N = 77.6\,\frac{p}{T} + 3.73 \times 10^5\,\frac{e}{T^2}$$

where p is the pressure of the atmosphere in hPa, T is the air temperature in K, and e is the water vapor pressure in hPa.

Data quality control

Three steps are involved in the quality control of refractivity (N) data: the gross error check, the percent error check, and the vertical gradient check. Each observation from a profile at different levels is treated as independent. In the gross error check, an observation is discarded if the difference between the observation and the model background exceeds a predefined threshold. In this study, the threshold is set at five times the sensor error, which is commonly used in assimilation research (Singh et al. 2021). The percent error check rejects an observation if the percentage of the differences between the observation and the model background refractivity exceeds the predefined threshold, which varies at different heights. The threshold values are 5% for below 7 km, 4% for 7–25 km, and 10% for above 25 km (Cucurull et al. 2007). The vertical gradient check assesses the gradient of the refractivity to identify anomalous values. An observation is discarded if dN/dz is less than -50 km^{-1} or if the absolute d^2N/dz^2 is larger than 100 km^{-2} (Poli et al. 2009).

Experiment design

The numerical experiments conducted in this study utilize the three-dimensional and non-hydrostatic Weather Research and Forecasting (WRF) version 4.3 as the forecast model (Skamarock et al. 2008). The WRF Data Assimilation (WRFDA) of the three-dimensional framework (3DVAR) is used for assimilation (Barker et al. 2004). The model domain covers most areas of China, with Henan located at the center of the domain (Fig. 2). The horizontal resolutions of the model are 15 km for the outer domain (250 × 250) and 5 km for the inner domain (300 × 300). In our 2-way nesting simulations, the outer domain provides boundary conditions to the inner domain for further simulations. In the vertical direction, there are 45 model layers with a model top of 50 hPa. The physics

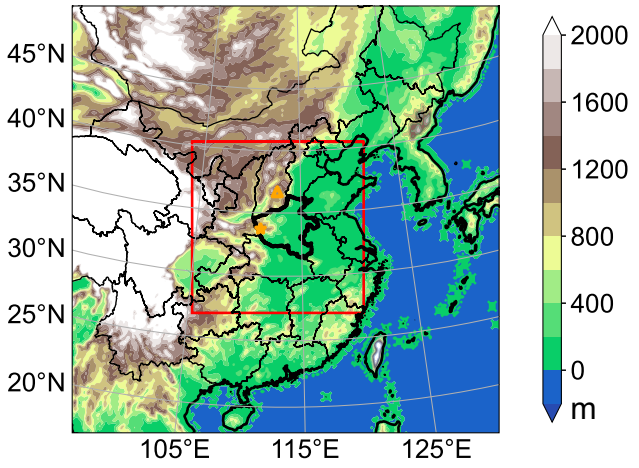

Fig. 2 Topography of the simulation domains. The red frame denotes the inner domain. The bold lines inside the red frame denote the location of Henan

schemes employed in this study are the Tiedtke Scheme for cumulus physics (Tiedtke 1989), the Thompson scheme for microphysics (Thompson et al. 2008), the Yonsei university scheme (YSU) for planetary boundary layer physics (Hong et al. 2006), the Noah-MP land surface model (Yang et al. 2011), RRTMG shortwave and longwave schemes (Iacono et al. 2008).

Three experiments are carried out in this study: CNTL, RO, and RO + GNOS. The experiment CNTL assimilates conventional data from GTS, including reports from radiosondes, surface observations, pilot balloons, and aircraft data. The experiment RO is identical to CNTL, except for the assimilation of GNSS radio occultation refractivity data from COSMIC-2 and MetOp. In addition to the GNSS radio occultation refractivity used in RO, the experiment RO + GNOS assimilates the radio occultation refractivity data obtained from GNOS onboard FY-3C. All assimilations are executed at a 6-h assimilation window (three hours ahead and three hours after). Background fields are obtained by 6-h WRF forecasts that are initialized from GFS data. These 6-h forecasts help to reduce the initial dynamic imbalance that could impede the assessment of the data's impacts (Wee et al. 2014). After the assimilation, 72-h forecasts are produced for all of these three experiments.

Fractions skill scores (FSS)

In this study, we use fractions skill scores (FSS) to evaluate the accuracy of precipitation forecasts. FSS is a scale-selective method designed to measure the skill of high-resolution forecast of precipitation, using the nearest neighbors to select the scales and thresholds of interest (Lean and Roberts 2008), and is defined as:

$$\mathrm{FSS} = 1 - \frac{\mathrm{FBS}}{\mathrm{FBS}_{\mathrm{w}}} \tag{1}$$

where *FBS* is the fractional Brier score (Brier 1950), and $\mathrm{FBS}_{\mathrm{w}}$ is the worst FBS when there is no overlap of nonzero fractions (Coniglio et al. 2009). They are calculated by

$$\mathrm{FBS} = \frac{1}{N}\sum_{i=1}^{N}\left[P_{\mathrm{F}(i)} - P_{\mathrm{O}(i)}\right]^2 \tag{2}$$

$$\mathrm{FBS}_{w} = \frac{1}{N}\left[\sum_{i=1}^{N}P_{\mathrm{F}(i)}^2 + \sum_{i=1}^{N}P_{\mathrm{O}(i)}^2\right] \tag{3}$$

where $P_{\mathrm{F}(i)}$ and $P_{\mathrm{O}(i)}$ are the fractional values exceeding the given thresholds at the *i*th grid of a predefined radius. *N* is the number of grids.

Results and analysis

In this section, we first conduct a 24-h forecast to examine the effect of GNSS radio occultation on predicting the forthcoming extreme rainfall. We assess the accuracy of the three experiments and provide potential meteorological explanations for the enhancements observed in RO + GNOS. Furthermore, we generate 48-h and 72-h forecasts to demonstrate the robustness of GNSS radio occultation in predicting this Henan rainstorm.

Twenty-four-hour forecast of extreme rainfall

Figure 3 exhibits the fractional differences of refractivity between model profiles and observations before and after assimilating the GNSS radio occultation sounding at (48.44°N, 101.90°E) at 1200 UTC on July 19, as an example of modifications made to the model background. Before assimilating this sounding, there are relatively large fractional differences between the observation and model background. Below 4 km, the fractional differences are large, with a maximum of 6.93%. From 4–7 km, the negative fractional differences range from -2.09% to 0. Above 7 km, both profiles show small fractional differences within 2.00%. After assimilation, the model analysis is effectively improved throughout the entire profile. The fractional differences are all less than 1.00% above 4 km and are distinctly smaller than the model background below 4 km. Overall, the mean fractional difference decreases from 1.85 to 1.34%.

Figure 4 shows the temperature and moisture increments between the CNTL experiment and the RO and RO + GNOS experiments at the initial time of 1200 UTC on July 19. At 500 hPa, RO produces higher temperatures and geopotential height over most areas, with two radio occultation soundings directly influencing the initial thermal conditions and causing strong baroclinicity at the north (35.65°N, 112.89°E)

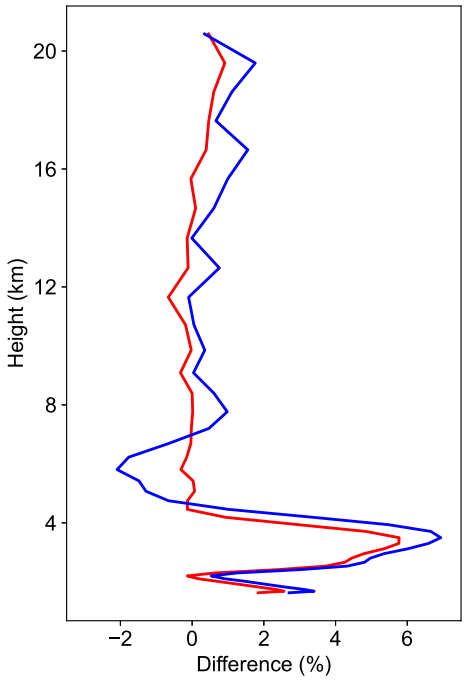

Fig. 3 Vertical variations of fractional differences of refractivity between the observation and model background (blue) as well as the observation and model analysis (red)

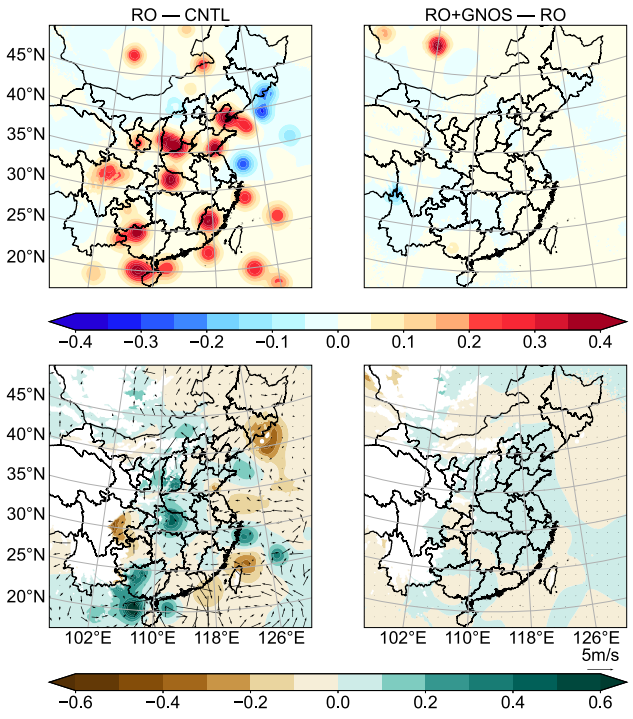

Fig. 4 Increments of different meteorological variables for RO (left) and RO + GNOS (right) at 1200 UTC on July 19. Top panel: temperature, geopotential height at 500 hPa. Bottom panel: specific humidity, wind vectors at 850 hPa for RO

and south (31.48°N, 111.91°E) of Henan. The maximum increment in temperature is 0.51 K and 0.41 K, respectively. At 850 hPa, RO intensifies the moisture conditions at several key locations, with specific humidity enhancements of up to 0.422 g/kg and 0.488 g/kg at the north and south of Henan, respectively. Moreover, the water vapor channels developed by typhoons In-Fa and Cempaka are much more distinct and precise in RO, providing abundant moisture for the extreme rainfall in Henan. The main differences between RO + GNOS and RO are triggered by additional GNOS radio occultations at (48.44°N, 101.90°E), (48.64°N, 90.92°E), and (28.98°N, 99.21°E). The increments of temperature at 500 hPa are distinct. But there are blanks in humidity increments at 850 hPa due to the presence of high mountains in these areas. Although the three radio occultation profiles are relatively far from Henan, their differences can still influence the forecast results as the synoptic system moves over hours of model integration.

After obtaining a more accurate initial condition by assimilating GNSS radio occultation soundings, it is intriguing to find out whether the rainfall prediction is improved. Figure 5A shows the 24-h accumulated precipitation during 1200 UTC on July 19–20, 2021, for both observation and simulations. The observed rainfall was mostly concentrated in the north of central Henan, covering an extensive area where rainfall exceeded 200 mm, with the maximum accumulated precipitation of 552.5 mm at Zhengzhou (34.71°N, 113.66°E). Generally, CNTL successfully predicts the distribution of moderate rain (25–50 mm) and the occurrence of a heavy downpour (larger than 200 mm), but the center of the rainstorm is slight to the west, and its intensity is much underestimated, with only a narrow area predicted to receive more than 200 mm of precipitation. The maximum accumulated precipitation of 481.24 mm is located at (34.35°N, 112.00°E), which is far from the observation. RO shows a similar precipitation pattern with CNTL, but the rainfall is more concentrated, and the false precipitation outside the northwest of Henan disappears, with the area of more than 100 mm of precipitation being much larger. Moreover, the entire precipitation system is a bit more to the east, and the location of maximum accumulated precipitation (34.22°N, 113.16°E) is closer to observation. For RO + GNOS, the distributions of torrential rain (50–100 mm) and downpour (100–200 mm) are similar to RO. Their main difference is in the distribution of heavy downpours (larger than 200 mm), and the area of heavy downpours in RO + GNOS is 8.40% larger than in RO. In terms of the time series of precipitation for the location with the maximum accumulated precipitation (Fig. 5B), the most intense rainfall occurred in Zhengzhou between 0600–0900 UTC on July 20, with a total amount of 274.8 mm in three hours. CNTL fails to predict the time for rainfall accurately. It overpredicts the rainfall from 2100 UTC on July 19–0300 UTC on July 20 and does

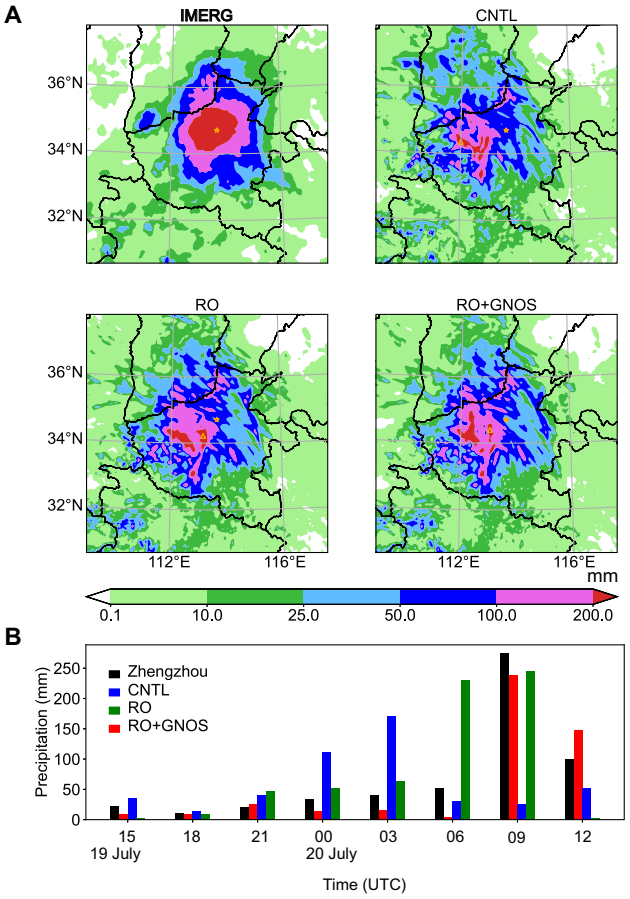

Fig. 5 **A:** Twenty-four-hour accumulated rainfall during 1200 UTC July 19–20 2021 for IMERG observation (top left), CNTL (top right), RO (bottom left), and RO + GNOS (bottom right). Yellow stars indicate the location of Zhengzhou and yellow triangles indicate the locations of simulated maximum accumulated rainfall. **B:** Time series of 3-hourly accumulated rainfall at Zhengzhou and the locations of maximum accumulated rainfall for CNTL, RO, and RO + GNOS

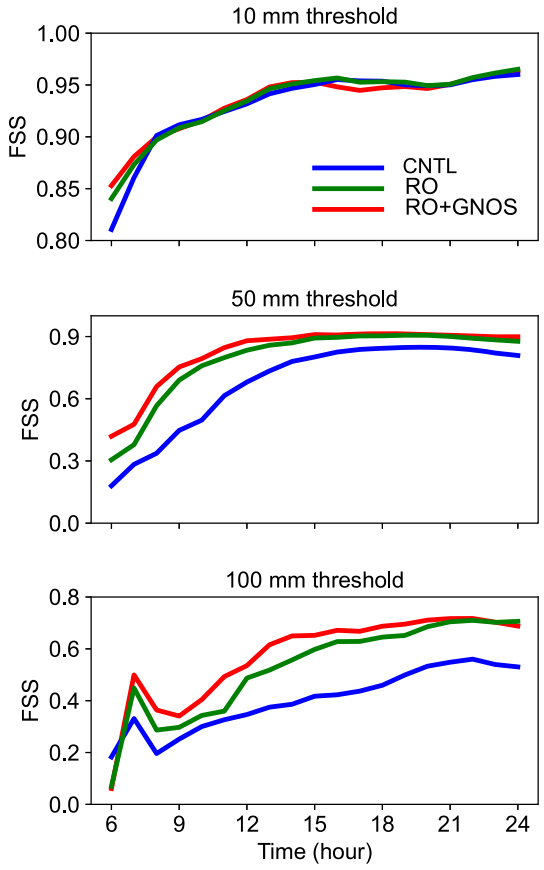

Fig. 6 FSSs of hourly-accumulated precipitation using a 50 km radius of influence, with thresholds of 10 mm (top), 50 mm (middle), and 100 mm (bottom), initialized at 1200 UTC on July 19

not forecast the heavy downpour between 0600–0900 UTC on July 20. RO agrees best with the observed precipitation between 0600–0900 UTC on July 20 but falsely predicts heavy rainfall between 0300–0600 UTC on July 20. Therefore, RO + GNOS produces the best overall consistency with the observation. Its averaged 3-hourly root-mean-square error (RMSE) was reduced by 71.6% and 60.0% against CNTL and RO, respectively. These results suggest that GNSS radio occultation data contributed to the prediction of the July 2021 Henan Extreme Heavy Rainstorm in terms of rainfall distribution, amount, and the time of extreme rainfall onset.

Accuracy of hourly precipitation prediction

To explicitly assess the performance for the prediction of different thresholds, we employed FSS to quantify the forecast skills. The FSS reflects the accuracy of predicted rainfalls exceeding a given threshold, compared to observations over neighborhoods. The scores of FSS range from 0 to 1, where 0 represents the worst and 1 is the best. Figure 6 shows the FSSs of hourly accumulated precipitation at 10, 50, and 100 mm thresholds with a radius of 50 km, initialized at 1200 UTC on July 19. The FSS calculation starts from the sixth hour after the initial time, since the predictions need some spin-up time and the outputs at the first several hours are not entirely reliable. Overall, the RO outperforms CNTL, and RO + GNOS achieves the highest score for all three thresholds. For the 10 mm threshold, RO and RO + GNOS show little improvement between the 6^{th}–8^{th} hour and have no conspicuous advantage after that because the most precipitation region has already reached the thresholds after the hours of amassment. Yet, there are substantial enhancements in RO and RO + GNOS for 50 mm and 100 mm thresholds. The improvements with minimum, maximum, and average values are given in Table 1.

The reason why RO + GNOS outperforms RO and CNTL is worth further exploring, thus we illustrate domain-mean RMSEs of specific humidity, temperature, and wind vectors

Table 1 Improvements of RO and RO + GNOS compared with CNTL (%)

	10 mm	50 mm	100 mm (except for the 7th hour)
	Minimum		
RO	− 0.481	6.68	10.2
RO + GNOS	− 0.962	7.34	28.0
	Maximum		
RO	3.67	69.7	48.5
RO + GNOS	5.22	133	85.6
	Mean		
RO	0.381	23.0	33.4
RO + GNOS	0.373	32.6	47.4

for CNTL, RO, and RO + GNOS at 0800 UTC on July 20 (Fig. 7), which is the beginning of maximum hourly rainfall. The three experiments show similar profiles for specific humidity. On the whole, the RMSEs are small in the upper layers and gradually increase downward. They reach their maxima of more than 1.70 g/kg around 900 hPa and then decrease toward the ground. Their main differences are near 500 hPa and below 800 hPa, where RO and RO + GNOS show fairly smaller RMSEs compared with CNTL. Averagely, RO and RO + GNOS have a reduction of 0.076 g/kg and 0.082 g/kg compared with CNTL, respectively. As for temperature, all three experiments have similar small RMSEs along the entire profiles, except for relatively large RMSEs near the surface. RO and RO + GNOS exhibit no significant differences. But compared with CNTL, they have marked improvements above 500 hPa and near the surface. This temperature improvement in the mid-upper troposphere plays an important role in providing more accurate unstable conditions for the onset of rainfall. Different from specific humidity and temperature, the three experiments have large discrepancies in wind vectors, and there are no conspicuous changing rules. Overall, CNTL exhibits the largest averaged RMSEs for east–west and north–south wind components, followed by RO and RO + GNOS. More specifically, RO + GNOS have smaller RMSEs for the east–west wind component at almost all levels. While for the north–south wind component, RO + GNOS has smaller RMSEs than RO above 400 hPa but larger RMSEs below. These discrepancies in wind vectors are likely to be the main factor contributing to the differences in the above precipitation forecast.

Figure 8 shows the 850-hPa water vapor flux from ERA5 reanalysis at 0800 UTC on July 20, as well as the results of the three experiments. CNTL, RO, and RO + GNOS exhibit similar patterns and are spatially well-correlated with ERA5 reanalysis, where substantial amounts of water vapor are transported from the southeast. However, their main differences lie in the locations of maximum water vapor flux, and

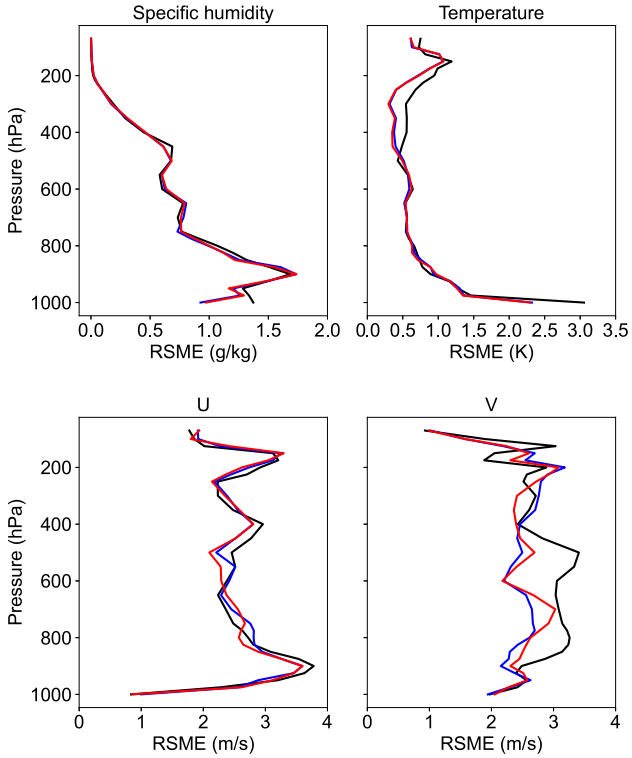

Fig. 7 RMSEs of specific humidity (top left), temperature (top right), east–west wind component (bottom left), and north–south wind component (bottom right) for CNTL (black), RO (blue), and RO + GNOS (red), at 0800 UTC on July 20

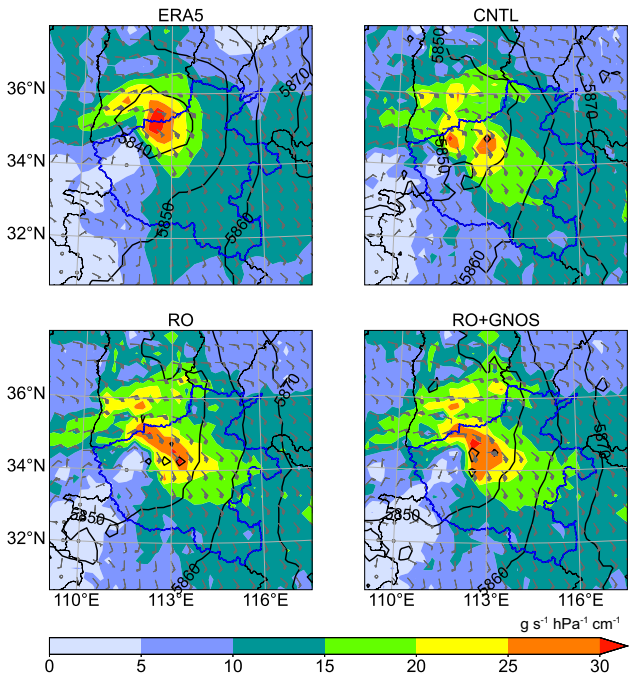

Fig. 8 Water vapor flux at 850 hPa and geopotential height (contours; gpm) at 500 hPa for ERA5 (top left), CNTL (top right), RO (bottom left), RO + GNOS (bottom right) at 0800 UTC on July 20

the strong wind shear at Taihang mountains (which marks the boundary of northwest Henan) results in the amassment of moisture. In ERA5 reanalysis, the maximum water vapor flux is located at the northwest boundary of Henan, accompanied by a strong low-pressure center. However, all three experiments show a slightly southeasterly center of water vapor flux, with a weaker and more localized low-pressure center. For experiment CNTL, the magnitude and spatial extent of strong water vapor flux are relatively smaller than those of RO and RO + GNOS. The primary difference between RO and RO + GNOS is that RO displays a banding distribution of strong water vapor flux, while the distribution of strong water vapor flux in RO + GNOS is more centered. Additionally, the water vapor flux convergence reflects the localized net income and expenses of water vapor. Figure 9 shows the RMSEs of water vapor flux convergence for CNTL, RO, and RO + GNOS in Henan. Generally, CNTL has the largest RMSEs compared with RO and RO + GNOS. RO + GNOS shows nearly the same variations of water vapor flux convergence as RO at the first 12 h. After that, RO + GNOS gradually exhibits a slight difference and has an exceptionally small RMSE at 0800 UTC on July 20. Its mean RMSEs reduce by 13.7% and 2.41% compared to CNTL and RO, respectively.

Forty-eight-hour and seventy-two-hour forecast

It is arbitrary to declare the triumph of GNSS radio occultation for the prediction of the July 2021 Henan extreme heavy rainstorm merely based on a single 24-h forecast run. Therefore, we extend two additional runs (a 48-h forecast initialed at 1200 UTC July 18 and a 72-h forecast initialed at 1200 UTC July 17) to provide further evidence of the effectiveness of GNSS radio occultation data (Fig. 10A). For the 48-h precipitation during 1200 UTC July 18–20, the observed rainfall center was located at Zhengzhou, and the accumulated precipitation decreased from the center to the periphery. The three experiments produced similar patterns and have good consistency with the observation regarding

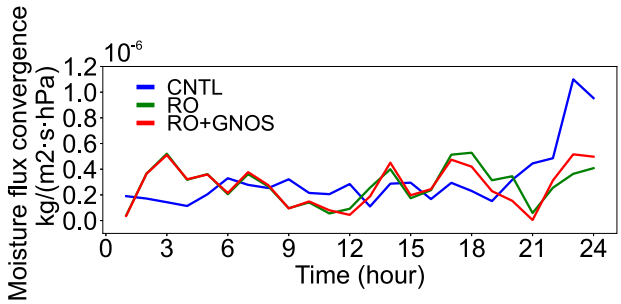

Fig. 9 RMSEs of water vapor flux convergence for CNTL (blue), RO (green), and RO + GNOS (red) forecast against the ERA5 reanalysis, initialized at 1200 UTC on July 19

the 50 and 100 mm rainbands. However, they all underpredict the area with over 200 mm of precipitation, despite RO and RO + GNOS having a larger coverage than CNTL. For the location of maximum accumulated precipitation, RO + GNOS outperforms CNTL and RO with remarkable accuracy. The time series of 6-hourly accumulated precipitation for the maximum accumulated precipitation is shown in Fig. 10B. Generally, RO + GNOS significantly reduces errors compared to CNTL and RO. CNTL severely underpredicts the intensity of rainfall, while RO overpredicts its intensity, and the predicted extreme rainfall is 12 h earlier than the observed rainfall peak. In contrast, RO + GNOS not only accurately predicts the timing of the rainfall peak but also produces a considerably accurate amount. For the 72-h precipitation during 1200 UTC July 17–20, the observed accumulated precipitation changes little as the rainfall principally developed during July 19–20, and all three experiments agree with the observation at the center of Henan. CNTL produces an excellent forecast result that is similar in pattern to the observation for areas with precipitation of 0.1, 1, 10, 25, 50, and 100 mm thresholds, except for a false strong rainfall center near the south of Henan. RO and RO + GNOS seem to show similar distributions but have many disparities. In detail, areas with precipitation below 100 mm are almost identical between RO and RO + GNOS, while the areas of 100 and 200 mm precipitation thresholds are quite different. RO exhibits a north–south banding distribution from north Henan to south-central Henan, while RO + GNOS displays a concentrated region for larger than 100 mm of precipitation, which is better consistent with observation. All three experiments underpredict precipitation larger than 200 mm, but CNTL and RO + GNOS produce relatively accurate locations for maximum accumulated precipitation with errors of 46.6 and 20.5 km, respectively. The time series of precipitation for the maximum accumulated precipitation is coarsened to 12 h to limit the uncertainty for the relatively long validation time. All three experiments predict the right time interval for extreme rainfall, but CNTL overpredicts it for 598.2 mm (28.41% of relative error), while RO underpredicts it by only 252.1 mm (45.87% of relative error). RO + GNOS is remarkably precise, with only a 5.247% relative error compared to observation.

Discussion

This study gives improvements in the prediction of the Henan extreme heavy rainstorm through the assimilation of GNSS radio occultation data and shows the preliminary impact of GNOS. However, there are several potential uncertainties and limitations in our research that require further investigation in future studies.

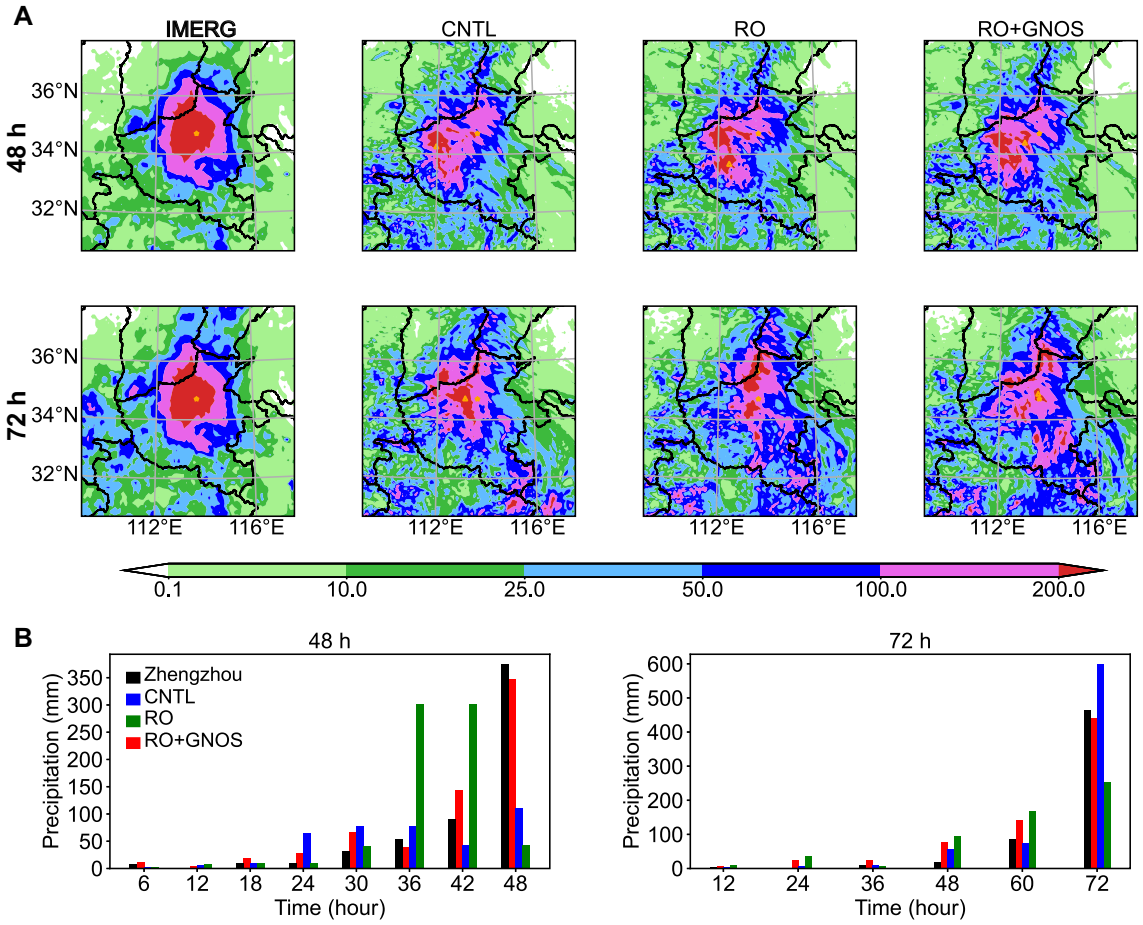

Fig. 10 **A** Results of 48-h (top panel) and 72-h (bottom panel) accumulated rainfall for IMERG observation, CNTL, RO, and RO + GNOS during 1200 UTC on July 18–20. Yellow stars indicate the location of Zhengzhou and yellow triangles indicate the locations of simulated maximum accumulated rainfall. **B** Time series of 6-hourly accumulated rainfall during 1200 UTC July 18–20 (left) and 12-hourly accumulated rainfall during 1200 UTC July 17–20 (right) at Zhengzhou (black) and the locations of maximum accumulated rainfall for CNTL (blue), RO (green), and RO + GNOS (red)

Firstly, both RO and RO + GNOS exhibit increased water vapor increments after assimilating GNSS radio occultation data, thereby the initial conditions are closer to observation at the moisture field. However, despite these improvements, both experiments still exhibit false precipitation around the rainfall center. This could potentially be attributed to the inner grid spacing of 5 km used in our experiments, which poses a great challenge for cumulus schemes in such a high-resolution model with grid spacing on the order of 1–10 km (Kain 2004). Thus, more powerful physics schemes suitable for high-resolution models need to be developed, and various physics suites warrant further investigation. Secondly, the complex topography in Henan plays a crucial role in this extreme rainstorm (Yin et al. 2022). As topography can significantly affect the physical process (Pontoppidan et al. 2017), future research could explore the use of finer-resolution topography data.

Furthermore, this study implements a local refractivity operator, balancing computational cost and horizontal errors. However, other operators like nonlocal refractivity and bending angle operators have been widely used in other research and are expected to outperform the local operator at high resolution (Caya et al. 2008). Nonetheless, Ma et al. (2009) pointed out that the nonlocal refractivity operator only yields limited improvements in certain experiments, and its superiority in predicting extreme rainstorms remains unclear.

In addition, more detailed studies can be carried out in the future. For example, the robustness of GNSS radio occultation and data from GNOS need to be verified in more extreme rainfall cases. Also, their performance in other types of atmospheric systems can be further investigated. Besides, other GNSS-based data, like GNSS PW, can be utilized simultaneously to obtain more accurate moisture conditions

at the lower troposphere, which may further improve the skill of extreme rainfall prediction.

Conclusions

In this study, we implemented GNSS radio occultation assimilation in the WRFDA 3DVAR system to estimate its impact on the extreme rainstorm event that occurred on July 20, 2021, in Henan. Retrospective studies are conducted for 24-h, 48-h, and 72-h forecasts validated at 1200 UTC on July 20. A set of forecasting experiments with and without GNSS radio occultation data assimilation is produced, and performances of GNSS radio occultation data from COSMIC-2, MetOp-A/B/C, and additional data from FY-3C are assessed.

The local refractivity operator positively contributes to the analysis fields for this extremely heavy rainstorm. Two influential radio occultation soundings near Henan directly magnified the initial moisture conditions for the 24-h forecast. Also, the specific humidity increments suggest two explicit water vapor channels established by typhoons In-Fa and Cempaka, which provide continuous extensive moisture for the forthcoming rainfall. The better initial condition leads to an improved forecast for this severe rainstorm. RO + GNOS exhibits the best performance for the distribution, amount, and timing of extreme rainfall onset, followed by RO and CNTL. The FSSs of hourly accumulated precipitation indicate that RO and RO + GNOS have noticeable advantages in predicting heavy rainstorms at thresholds of 50 mm and 100 mm, on account of more accurate moisture conditions. The 48-h and 72-h forecasts exhibit similar improvements, with RO + GNOS outperforming RO and CNTL regarding the distribution and amount of precipitation. In general, the additional soundings from FY-3C in RO + GNOS have beneficial impacts on the prediction of the extremely heavy Henan rainstorm, even though they were not located directly over Henan.

Furthermore, it is found that RO and RO + GNOS have small average RSMEs for temperature, specific humidity, and wind vectors at 0800 UTC on July 20, compared to CNTL. Although there is no conspicuous difference between RO and RO + GNOS for temperature and specific humidity, their discrepancies in wind vectors result in different distributions of water vapor flux and its convergence, which play important roles in the trigger conditions for the rainstorm and contribute to the main differences of precipitation between RO and RO + GNOS. Thus, RO + GNOS performs better than RO and CNTL, particularly in terms of the maximum amount of rainfall, owing to the enhanced wind forecast.

Acknowledgements This work made use of the High-Performance Computing Resource in the Core Facility for Advanced Research Computing at Shanghai Astronomical Observatory, CAS, China. This work was supported by the Strategic Priority Research Program Project of the Chinese Academy of Sciences (Grant No. XDA23040100).

Author contributions Yu Wang performed the experiments and wrote the manuscript. Shuanggen Jin helped edit the manuscript and perform the analysis with constructive suggestion. All authors reviewed the manuscript.

Funding Strategic Priority Research Program Project of the Chinese Academy of Sciences,XDA23040100

Data availability The IMERG precipitation products can be freely downloaded from NASA Global Precipitation Measurement Mission, https://gpm.nasa.gov/. The ERA5 reanalysis data can be freely downloaded from ECWMF, https://www.ecmwf.int/. The GFS and GTS products can be freely downloaded from NCAR Research Data Archive, https://rda.ucar.edu/datasets/. The GNSS radio occultation from COSMIC-2, MetOp-A/B/C, and FY-3C can be freely downloaded from https://data.cosmic.ucar.edu, https://www.romsaf.org/, and https://satellite.nsmc.org.cn/, respectively.

Declarations

Conflict of interest The authors declare no competing interests.

References

Anisetty SKAVP, Huang CY, Chen SY (2013) Impact of FORMOSAT-3/COSMIC radio occultation data on the prediction of super cyclone Gonu (2007): a case study. Nat Hazard 70(2):1209–1230. https://doi.org/10.1007/s11069-013-0870-0

Anthes RA (2011) Exploring Earth's atmosphere with radio occultation: contributions to weather, climate and space weather. Atmos Meas Tech 4(6):1077–1103. https://doi.org/10.5194/amt-4-1077-2011

Anthes R, Schreiner W (2019) Six new satellites watch the atmosphere over earth's equator. Eos. 100. DOI: https://doi.org/10.1029/2019eo131779

Bai WH, Sun YQ, Du QF, Yang GL, Yang ZD, Zhang P, Bi YM, Wang XY, Cheng C, Han Y (2014) An introduction to the FY3 GNOS instrument and mountain-top tests. Atmos Meas Tech 7(6):1817–1823. https://doi.org/10.5194/amt-7-1817-2014

Barker DM, Huang W, Guo YR, Bourgeois AJ, Xiao QN (2004) A three-dimensional variational data assimilation system for MM5: implementation and initial results. Mon Weather Rev 132(4):897–914. https://doi.org/10.1175/1520-0493(2004)132%3c0897:Atvdas%3e2.0.Co;2

Berg P, Moseley C, Haerter JO (2013) Strong increase in convective precipitation in response to higher temperatures. Nat Geosci 6(3):181–185. https://doi.org/10.1038/ngeo1731

Bi Y, Yang Z, Zhang P, Sun Y, Bai W, Du Q, Yang G, Chen J, Liao M (2012) An introduction to China FY3 radio occultation mission and its measurement simulation. Adv Space Res 49(7):1191–1197. https://doi.org/10.1016/j.asr.2012.01.014

Brier GW (1950) Verification of forecasts expressed in terms of probability. Mon Weather Rev 78(1):1–3. https://doi.org/10.1175/1520-0493(1950)078%3c0001:Vofeit%3e2.0.Co;2

Caya A, Snyder C, Kuo YH, Anderson J, Liu H (2008) Evaluation of a nonlocal quasi-phase observation operator in assimilation of

CHAMP radio occultation refractivity with WRF. Mon Weather Rev 136(1):242–256. https://doi.org/10.1175/2007mwr2042.1
Chen SY, Huang CY, Kuo YH, Guo YR, Shiau S (2009) Assimilation of GPS refractivity from FORMOSAT-3/COSMIC using a nonlocal operator with WRF 3DVAR and its impact on the prediction of a typhoon event. Terr Atmos Ocean Sci 20(1):133–154. https://doi.org/10.3319/tao.2007.11.29.01(f3c)
Chen H, Sun J, Chen X, Zhou W (2012) CGCM projections of heavy rainfall events in China. Int J Climatol 32(3):441–450. https://doi.org/10.1002/joc.2278
Cheng J, Zhao Y, Zhi R, Feng G (2022) Analysis of the July 2021 extreme precipitation in Henan using the novel moisture budget equation. Theor Appl Climatol 149(1–2):15–24. https://doi.org/10.1007/s00704-022-04022-7
Chien FC, Kuo YH (2009) Impact of FORMOSAT-3/COSMIC GPS radio occultation and dropwindsonde data on regional model predictions during the 2007 Mei-yu season. GPS Solut 14(1):51–63. https://doi.org/10.1007/s10291-009-0143-2
Coniglio MC, Levit JJ, Thomas KW, Kong F, Bright DR, Xue M, Weiss SJ, Kain JS, Schwartz CS (2009) Next-day convection-allowing WRF model guidance: a second look at 2-km versus 4-km grid spacing. Mon Weather Rev 137(10):3351–3372. https://doi.org/10.1175/2009mwr2924.1
Cucurull L, Derber JC, Treadon R, Purser RJ (2007) Assimilation of global positioning system radio occultation observations into NCEP's global data assimilation system. Mon Weather Rev 135(9):3174–3193. https://doi.org/10.1175/mwr3461.1
Dong Z, Jin S (2018) 3-D water vapor tomography in Wuhan from GPS. BDS and GLONASS Observ Remote Sens 10(1):62. https://doi.org/10.3390/rs10010062
Ha JH, Lim GH, Choi SJ (2014) Assimilation of GPS radio occultation refractivity data with WRF 3DVAR and its impact on the prediction of a heavy rainfall event. J Appl Meteorol Clim 53(6):1381–1398. https://doi.org/10.1175/jamc-d-13-0224.1
Healy SB (2008) Forecast impact experiment with a constellation of GPS radio occultation receivers. Atmos Sci Lett 9(3):111–118. https://doi.org/10.1002/asl.169
Hersbach H, et al. (2018) ERA5 hourly data on pressure levels from 1959 to present. Copernicus Climate Change Service (C3S) Climate Data Store (CDS). DOI: https://doi.org/10.24381/cds.bd0915c6
Ho SP et al (2020) The COSMIC/FORMOSAT-3 radio occultation mission after 12 years: accomplishments, remaining challenges, and potential impacts of COSMIC-2. Bull Am Meteorol Soc 101(7):E1107–E1136. https://doi.org/10.1175/bams-d-18-0290.1
Hong SY, Noh Y, Dudhia J (2006) A new vertical diffusion package with an explicit treatment of entrainment processes. Mon Weather Rev 134(9):2318–2341. https://doi.org/10.1175/mwr3199.1
Huang CY, Kuo YH, Chen SH, Vandenberghe F (2005) Improvements in typhoon forecasts with assimilated GPS occultation refractivity. Weather Forecast 20(6):931–953. https://doi.org/10.1175/waf874.1
Huffman GJ, Stocker EF, Bolvin DT, Nelkin EJ, Tan J (2019) GPM IMERG final precipitation L3 Half Hourly 0.1 degree x 0.1 degree V06. goddard earth sciences data and information services center.
Iacono MJ, Delamere JS, Mlawer EJ, Shephard MW, Clough SA, Collins WD (2008) Radiative forcing by long-lived greenhouse gases: calculations with the AER radiative transfer models. J Geophys Res 113:13. https://doi.org/10.1029/2008jd009944
Jin S, Su K (2020) PPP models and performances from single- to quad-frequency BDS observations. Satell Navig 1(1):16. https://doi.org/10.1186/s43020-020-00014-y
Jin S, Gao C, Li J (2019) Atmospheric sounding from fengyun-3C GPS radio occultation observations: first results and validation. Adv Meteorol 2019:1–13. https://doi.org/10.1155/2019/4780143
Jin S, Wang Q, Dardanelli G (2022) A review on multi-GNSS for earth observation and emerging applications. Remote Sens 14(16):3930. https://doi.org/10.3390/rs14163930
Jin S, Zhang T (2016) Terrestrial water storage anomalies associated with drought in southwestern USA from GPS observations. Surv Geophys 37(6):1139–1156. https://doi.org/10.1007/s10712-016-9385-z
Kain JS (2004) The Kain-Fritsch convective parameterization: an update. J Appl Meteorol 43(1):170–181. https://doi.org/10.1175/1520-0450(2004)043%3c0170:Tkcpau%3e2.0.Co;2
Kimura R (2002) Numerical weather prediction. J Wind Eng Ind Aerodyn 90(12–15):1403–1414. https://doi.org/10.1016/s0167-6105(02)00261-1
Kursinski ER, Hajj GA, Leroy SS, Herman B (2000) The GPS radio occultation technique. Terr Atmos Ocean Sci 11(1):53–114. https://doi.org/10.3319/tao.2000.11.1.53(cosmic)
Lean HW, Roberts NM (2008) Scale-selective verification of rainfall accumulations from high-resolution forecasts of convective events. Mon Weather Rev 136(1):78–97. https://doi.org/10.1175/2007mwr2123.1
Leith CE (1978) Objective methods for weather prediction. Annu Rev Fluid Mech 10(1):107–128. https://doi.org/10.1146/annurev.fl.10.010178.000543
Lenderink G, van Meijgaard E (2008) Increase in hourly precipitation extremes beyond expectations from temperature changes. Nat Geosci 1(8):511–514. https://doi.org/10.1038/ngeo262
Ma Z, Kuo YH, Wang B, Wu WS, Sokolovskiy S (2009) Comparison of local and nonlocal observation operators for the assimilation of GPS RO data with the NCEP GSI system: an OSSE study. Mon Weather Rev 137(10):3575–3587. https://doi.org/10.1175/2009mwr2809.1
Poli P, Moll P, Puech D, Rabier F, Healy SB (2009) Quality control, error analysis, and impact assessment of FORMOSAT-3/COSMIC in numerical weather prediction. Terr Atmos Ocean Sci 20(1):101–113. https://doi.org/10.3319/tao.2008.01.21.02(f3c)
Pontoppidan M, Reuder J, Mayer S, Kolstad EW (2017) Downscaling an intense precipitation event in complex terrain: the importance of high grid resolution. Tellus a: Dyn Meteorol Oceanogr. https://doi.org/10.1080/16000870.2016.1271561
Prein AF, Rasmussen RM, Ikeda K, Liu C, Clark MP, Holland GJ (2016) The future intensification of hourly precipitation extremes. Nat Clim Change 7(1):48–52. https://doi.org/10.1038/nclimate3168
Privé NC, Errico RM (2013) The role of model and initial condition error in numerical weather forecasting investigated with an observing system simulation experiment. Tellus a: Dyn Meteorol Oceanogr. https://doi.org/10.3402/tellusa.v65i0.21740
Rhys HJ, Seth W, Ashish S (2010) Observed relationships between extreme sub-daily precipitation, surface temperature, and relative humidity. Geophys Res Lett 37(22):805. https://doi.org/10.1029/2010gl045081
Schreiner WS et al (2020) COSMIC-2 radio occultation constellation: first results. Geophys Res Lett 47:4. https://doi.org/10.1029/2019gl086841
Singh R, Ojha SP, Anthes R, Hunt D (2021) Evaluation and assimilation of the COSMIC-2 Radio occultation constellation observed atmospheric refractivity in the WRF data assimilation system. J Geophys Res: Atmos 126:18. https://doi.org/10.1029/2021jd034935
Skamarock WC, Klemp JB, Dudhia J, Gill DO, Barker D, Duda MG, Powers JGDDSM (2008) A description of the advanced research WRF version 3. Univ Corp Atmos Res. https://doi.org/10.5065/D68S4MVH
Smith EK, Weintraub S (1953) The constants in the equation for atmospheric refractive index at radio frequencies. J Res Nat Bur Stand. https://doi.org/10.6028/jres.050.006

Thompson G, Field PR, Rasmussen RM, Hall WD (2008) Explicit forecasts of winter precipitation using an improved bulk microphysics scheme. Part II: implementation of a new snow parameterization. Mon Weather Rev 136(12):5095–5115. https://doi.org/10.1175/2008mwr2387.1

Tiedtke M (1989) A comprehensive mass flux scheme for cumulus parameterization in large-scale models. Mon Weather Rev 117(8):1779–1800. https://doi.org/10.1175/1520-0493(1989)117%3c1779:Acmfsf%3e2.0.Co;2

Trenberth KE, Dai A, Rasmussen RM, Parsons DB (2003) The changing character of precipitation. Bull Am Meteorol Soc 84(9):1205–1218. https://doi.org/10.1175/bams-84-9-1205

von Engeln A, Andres Y, Marquardt C, Sancho F (2011) GRAS radio occultation on-board of Metop. Adv Space Res 47(2):336–347. https://doi.org/10.1016/j.asr.2010.07.028

Wang Y, Li H, Wang H, Sun B, Chen H (2021) Evaluation of CMIP6 model simulations of extreme precipitation in China and comparison with CMIP5. Acta Meteor Sin 79(3):369–386. https://doi.org/10.11676/qxxb2021.031

Wee TK, Chen SY, Kuo YH, Bromwich DH (2014) An impact assessment of GPS radio occultation data on prediction of a rapidly developing cyclone over the southern ocean*. Mon Weather Rev 142(11):4187–4206. https://doi.org/10.1175/mwr-d-14-00024.1

Westra S, Alexander LV, Zwiers FW (2013) Global increasing trends in annual maximum daily precipitation. J Clim 26(11):3904–3918. https://doi.org/10.1175/jcli-d-12-00502.1

Wolff DB, Nelkin EJ, Bolvin DT, Huffman GJ, Adler RF, Gu G, Hong Y, Bowman KP, Stocker EF (2007) The TRMM Multisatellite Precipitation Analysis (TMPA): quasi-global, multiyear, combined-sensor precipitation estimates at fine scales. J Hydrometeorol 8(1):38–55. https://doi.org/10.1175/jhm560.1

Yang ZL et al (2011) The community Noah land surface model with multiparameterization options (Noah-MP): 2. Evaluation over global river basins. J Geophys Res 116:12. https://doi.org/10.1029/2010jd015140

Yin L, Ping F, Mao JH, Jin SG (2022) Analysis on precipitation efficiency of the "21.7" Henan extremely heavy rainfall event. Adv Atmos Sci 40:374–392. https://doi.org/10.1007/s00376-022-2054-x

Zhang W, Zhou T (2020) Increasing impacts from extreme precipitation on population over China with global warming. Sci Bull 65(3):243–252. https://doi.org/10.1016/j.scib.2019.12.002

Yu Wang is an M.Sc student and research assistant at Shanghai Astronomical Observatory, Chinese Academy of Sciences, Shanghai, China. His current research mainly focuses on GNSS meteorology, atmospheric remote sensing, climate change, and climate dynamics.

Shuanggen Jin is a Professor at Shanghai Astronomical Observatory, Chinese Academy of Sciences, China, Vice-President & Professor at Henan Polytechnic University, China, Member of Academia Europaea, Member of the European Academy of Science, Fellow of Electromagnetics Academy, Fellow of African Academy of Sciences, IUGG Fellow and IAG Fellow. He received a Ph.D. in Geodesy from the University of Chinese Academy of Sciences in 2003 and a B.Sc in Geodesy from Wuhan University in 1999. He has been active in Satellite Navigation, Space Geodesy, Remote Sensing, and Space/Planetary Exploration.